

# Polymerization-Induced Self-Assembly (PISA) - Control over the Morphology of $^{19}\text{F}$ -Containing Polymeric Nano-objects for Cell Uptake and Tracking

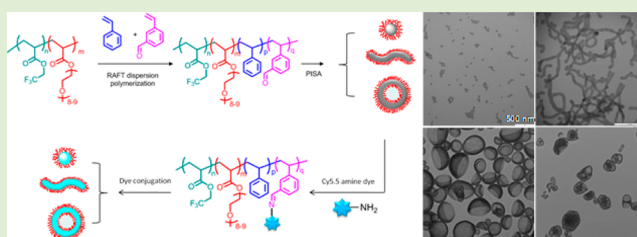
Wei Zhao,<sup>†,‡</sup> Hang T. Ta,<sup>†,‡</sup> Cheng Zhang,<sup>†,‡</sup> and Andrew K. Whittaker<sup>\*,†,‡,§</sup>

<sup>†</sup>Australian Institute for Bioengineering and Nanotechnology, The University of Queensland, Brisbane, St. Lucia, Queensland 4072, Australia

<sup>‡</sup>ARC Centre of Excellence in Convergent Bio-Nano Science and Technology, Brisbane, Queensland 4072, Australia

## S Supporting Information

**ABSTRACT:** Fluorine-containing polymeric materials are receiving increasing attention as imaging probes in fluorine-19 magnetic resonance imaging ( $^{19}\text{F}$  MRI), for example to enable quantitative *in vivo* detection of cells. Here we describe the one-pot polymerization synthesis of  $^{19}\text{F}$ -containing functional poly(oligo(ethylene glycol) methyl ether methacrylate-*co*-2,2,2-trifluoroethyl acrylate-*b*-poly(styrene-*co*-3-vinylbenzaldehyde) (poly(OEGA-*co*-TFEA)-*b*-poly(St-*co*-VBA)) copolymers as a new class of fluorinated MRI agent. A range of nanoparticle morphologies, including spheres, worm-like particles, and vesicles were formed as a consequence of polymerization-induced self-assembly (PISA). It was found that the extent of cell uptake strongly depends on the morphology of the nano-objects, with preferable uptake for worm-like particles compared to spherical nanoparticles and vesicles. All the nano-objects have a single resonance in the  $^{19}\text{F}$  NMR spectrum with relatively short MRI relaxation times, which were independent of the morphology of the nano-objects. These results confirm that these polymeric nano-objects of varied morphologies are promising as  $^{19}\text{F}$  MRI imaging agents for use in tracking of cells and selective MRI.



## INTRODUCTION

Magnetic resonance imaging (MRI) is a noninvasive imaging technique that can provide cross-sectional images with high contrast of solid tumors and surrounding tissues without exposure to hazardous radiation.<sup>1–3</sup> MRI is employed directly for imaging the ubiquitous  $^1\text{H}$  nuclei in the body.<sup>4</sup> MRI contrast agents (CAs) are, however, often required to enhance image contrast, and work by altering the relaxation properties of protons in water molecules within surrounding tissue in a manner that also depends on the MRI imaging sequence. Despite such relaxation agents having significantly improved the performance and utility of MRI, a number of limitations remain. For example, the high background signal from water and the intrinsic sources of contrast in tissue often prevent the discrimination of diseased tissue using  $^1\text{H}$  relaxation agents.<sup>5</sup> In addition, the changes in contrast induced by indirect modulation by the contrast agents of the water protons are not readily related to local concentration of the imaging agent in complex body conditions.<sup>6</sup> The alternative approach of directly observing the nuclear spins of the contrast agent, rather than the neighboring spins, has significant advantages if the objective is to quantitatively measure the local concentration of the CAs. This approach is, however, impractical if observing  $^1\text{H}$  spins, due to the overwhelming confounding signal from endogenous protons in the body.

The application of  $^{19}\text{F}$  MRI is one of the promising strategies to overcome these limitations, since the  $^{19}\text{F}$  MR signal arises only from the fluorine atoms contained within the  $^{19}\text{F}$  MRI CAs. In addition, fluorine ( $^{19}\text{F}$ ) presents comparable magnetic resonance sensitivity to protons, while exhibiting physiological rarity within the body, which minimizes an overwhelming background signal during imaging.<sup>7,8</sup> More importantly, thanks to the linear relationship between  $^{19}\text{F}$  concentration and resulting signal intensity,  $^{19}\text{F}$  has been recognized as a promising modality to complement  $^1\text{H}$  to achieve quantitative MRI.<sup>9,10</sup>

Multifunctional polymeric nanostructures, including spheres, worms, rods and vesicles, in combination with biological molecules, imaging agents, and prodrugs, are attractive assemblies, with significant potential for applications ranging from molecular imaging, delivery vehicles for therapeutics, and as precursors to nanosized microelectronic devices.<sup>11–13</sup> It is well-known that the morphology and the shape of nanosized particles affect their blood circulation time, as well as the rate and extent of uptake by cells,<sup>14–18</sup> which then influences their behavior and functionality and fate *in vivo*. These aspects are discussed in more detail below.

Received: December 1, 2016

Revised: March 23, 2017

Published: March 24, 2017

The most commonly used method to prepare such polymeric nanostructures is through the self-assembly of amphiphilic diblock copolymers, starting from a good solvent for both blocks followed by the slow addition of water (a poor solvent for the hydrophobic block) until attaining the required solvent ratio.<sup>19</sup> While this is a simple and convenient method to prepare nanoassemblies of polymers, the resultant self-assembled nano-objects are generally formed at low polymer concentrations (<1%), which makes the scale-up of production rather impractical. To address this limitation, a number of recent studies have proposed an approach based on a polymerization induced self-assembly process (termed "PISA") using living radical polymerization techniques such as reversible addition-fragmentation chain transfer (RAFT) polymerization.<sup>20,21</sup>

The combination of <sup>19</sup>F MRI and PISA techniques has the potential to contribute to several fields of biomedical research, in particular to the design of MRI agents, and to further our understanding of the factors affecting the uptake of particles by cells. This technique described here can create nano-objects with a partly fluorinated polymer comprising the corona in multiple morphologies through a one-pot reaction. Therefore, in this study we exploit the PISA approach to prepare a range of novel fluorinated diblock copolymer nano-objects. These were subsequently conjugated with a fluorescent dye for further *in vitro* cell culture studies. To ensure the successful formation of the nano-objects, as well as the appropriate fluorine content to provide strong <sup>19</sup>F signals, the structures of the fluorinated copolymers as macro CTA have been carefully designed and characterized. The effect of diblock copolymer morphology on the sensitivity of <sup>19</sup>F MRI imaging and on cell uptake and cell viability has been investigated in detail. The work described here will influence both the design of <sup>19</sup>F MRI agents, and nanoparticles for effective uptake by cells.

## EXPERIMENTAL SECTION

**Materials.** Oligo(ethylene glycol) methyl ether acrylate (OEGA<sub>480</sub>,  $M_n \approx 480 \text{ g mol}^{-1}$ ), 2,2,2-trifluoroethyl acrylate (TFEA, 99%, Sigma), 3-vinyl benzaldehyde (VBA, 98%, Sigma) and styrene (St, > 98%, Sigma) were purified by passing through basic alumina. 2,2'-Azobis[2-(2-imidazolin-2-yl)propane] dihydrochloride (VA-044, > 98%, Wako), 1, 1'-azobis(1-cyclohexane-carbonitrile) (VA-88, 98%, Aldrich) were used as received. The chain transfer agent 4-cyano-4-[(butylsulfanylthiocarbonyl)sulfanyl] pentanoic acid (CTBPA) was synthesized according to the literature method.<sup>22</sup> All the other reagents were used as purchased unless otherwise stated, and all reactions were carried out under argon atmosphere.

**Synthesis of Poly(OEGA-co-TFEA) macro-CTA via RAFT polymerization.** The <sup>19</sup>F-containing copolymer poly(OEGA-co-TFEA) was synthesized by RAFT polymerization in the presence of 4-cyano-4-[(butylsulfanylthiocarbonyl)sulfanyl] pentanoic acid (CTBPA) as chain transfer agent (CTA). A typical example of the procedure is as follows: OEGA (1.5 g, 3.13 mmol), TFEA (0.12 g, 0.78 mmol), VA-044 (1.01 mg, 0.0032 mmol), CTBPA (45.54 mg, 0.16 mmol), and H<sub>2</sub>O/1, 4-dioxane (80:20/m: m, 4 g) were added into a 25 mL flask fitted with a magnetic stir bar. The solution in the septum-sealed flask was purged for 20 min with argon and then heated to 60 °C in an oil bath under stirring. After 2 h, the polymerization was quenched by rapid cooling upon immersion of the flask in an iced water bath. The overall monomer conversion was determined by <sup>1</sup>H NMR spectroscopy in DMSO-*d*<sub>6</sub> by comparing the ratio of intensities of peaks from the vinyl protons of OEGA and TFEA centered at  $\delta$  5.7 (1H, dd) and  $\delta$  5.4 (1H, dd), to the alkyl proton peaks at  $\delta$  4.26 (2H, t) and 4.55 (2H, t) with their polymeric counterparts at  $\delta$  4.15 (2H, br) and 4.49 (2H, br), respectively. The polymer was purified by dialysis against Milli-Q water for 24 h and dried in a vacuum oven at

room temperature. The experimental molecular weight and dispersity were determined by size exclusion chromatography (SEC) in THF with PS as molecular weight standards ( $M_{n,SEC} = 10600 \text{ g mol}^{-1}$ ,  $\bar{D} = 1.10$ ). The resulting poly(OEGA-co-TFEA) was used as macro-CTA for further RAFT dispersion polymerization with additional St and VBA monomers.

**Calculation of  $M_{n,th}$ .** The theoretical number-average molecular weight ( $M_{n,th}$ ) was calculated using eq 1.<sup>23</sup>

$$M_{n,th} = \frac{[M]_0 p M_M}{[CTA]_0 + 2f[I]_0(1 - e^{-k_d t})\left(1 - \frac{f_c}{2}\right)} + M_{CTA} \quad (1)$$

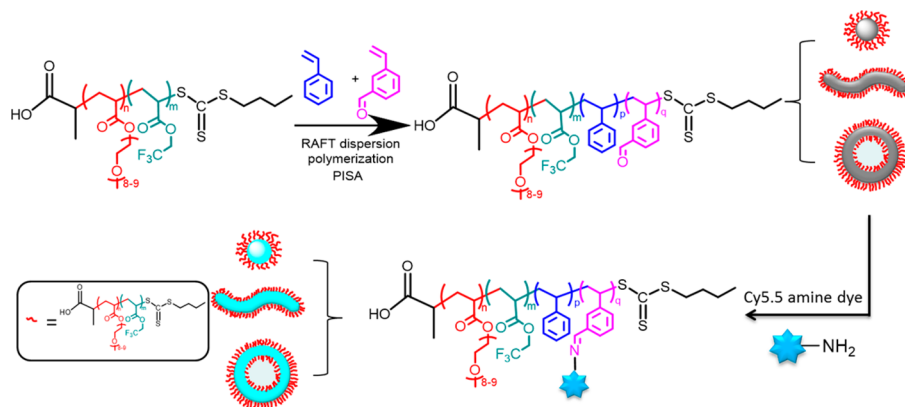
where  $[M]_0$ ,  $[CTA]_0$ , and  $[I]_0$  are the initial concentrations (in mol L<sup>-1</sup>) of the monomer, the chain transfer agent, and the initiator, respectively;  $p$  is the monomer conversion, as determined by <sup>1</sup>H NMR;  $M_M$  and  $M_{CTA}$  are the molar masses (in g mol<sup>-1</sup>) of the monomer and the chain transfer agent, respectively;  $k_d$  is the decomposition rate constant (in s<sup>-1</sup>) of the azo initiator; and  $t$  is the polymerization time (in seconds). The factor "2" accounts for the fact that one molecule of azo initiator yields two primary radicals with the efficiency  $f$  (assumed to be equal to 0.5 in this study). The decomposition rate constant for VA-044 at the temperature  $T$  ( $k_{d,VA-044(T)}$ ) was determined from the values obtained from Wako ( $k_{d,VA-044(44^\circ\text{C})} = 1.92 \times 10^{-5} \text{ s}^{-1}$  and  $E_a = 108\,000 \text{ J}\cdot\text{mol}^{-1}$ ) using the Arrhenius equation ( $k_{d,VA-044(60^\circ\text{C})} = 1.65 \times 10^{-4} \text{ s}^{-1}$ ). The term  $1 - (f_c/2)$  is equal to the number of chains produced in a radical-radical termination event with  $f_c$  being the coupling factor. An  $f_c$  value of 1 means that all bimolecular terminations occur by combination, whereas a value of 0 indicates that 100% of bimolecular terminations result in disproportionation. In this study, 100% termination by disproportionation is assumed ( $f_c = 0$ ).

**Calculation of the Theoretical Number Fraction of Living Chains ( $L$ ).** The number fraction of living chains was calculated using eq 2.<sup>23</sup>

$$L = \frac{[CTA]_0}{[CTA]_0 + 2f[I]_0(1 - e^{-k_d t})\left(1 - \frac{f_c}{2}\right)} \quad (2)$$

**Synthesis of Poly(OEGA-co-TFEA)-*b*-poly(St-co-VBA) Diblock Copolymer Nano-objects by RAFT Dispersion Polymerization.** Core-functional poly[(OEGA-co-TFEA)-*b*-poly(St-co-VBA) block copolymers with various morphologies were synthesized in isopropanol by RAFT dispersion polymerization with a molar feed ratio of St:VBA:poly[(OEGA-co-TFEA)]:VA-88 = 4750:250:1:0.1. In a typical experiment, poly[(OEGA-co-TFEA)] as a macro-CTA (0.054 g, 0.005 mmol), styrene (2.5 g, 24 mmol), VBA (0.167 g, 1.26 mmol) as a functional monomer and 1,1'-azobis(1-cyclohexanecarbonitrile) (VA-88, 0.123 mg, 0.0005 mmol) were dissolved in isopropanol (2.5 g, 48.8 wt %, styrene:isopropanol = 1:1/m:m). The reaction mixture was divided equally into five vials to study the kinetics of the reaction. Each vial was sealed carefully and gently purged with nitrogen for 10 min. The reaction mixtures were then immersed in an oil bath at 90 °C, and vials were taken out at specific time points, 3, 5, 7, 9 h. The polymerization was terminated by placing the reaction mixture into an ice-bath for 5 min and exposure to air. The polymer was purified three times by dialysis in methanol using a dialysis tube with a molecular weight cut off of 3500 (MWCO 3500 Da). Morphologies and number-average diameter of the block copolymers were investigated directly from the dispersion solution by diluting samples with methanol (2 mg/mL).

**Conjugation of Cy5.5 to Poly(OEGA-co-TFEA)-*b*-poly(St-co-VBA) Nano-objects.** In the presence of triethylamine (50  $\mu$ L), 20 mg of poly(OEGA-co-TFEA)-*b*-poly(St-co-VBA) and was dispersed in 2 mL Cy5.5 DMSO stock solution (0.1 mg/mL) and the mixture stirred at room temperature for 2 h. The mixture was first dialyzed (MWCO 3500 Da) against methanol for 24 h, and then against H<sub>2</sub>O for 48 h to remove solvent, trimethylamine, and free dye. The concentration of the polymers was determined by freeze-drying a known volume of the solution.

Scheme 1. Illustration of the Preparation of Fluorinated Polymeric Nano-objects for  $^{19}\text{F}$  MRI Contrast Agents

**Cell Cultures.** Chinese Hamster Ovarian (CHO) cells (passage 2–4) were used to investigate cell uptake and toxicity of the polymeric nanoparticles. Cells were grown in Dulbecco's Modified Eagle Medium (DMEM) supplemented with 10% fetal bovine serum albumin, 4.5 g/L glucose, 2 mM L-glutamine, 1% nonessential amino acids and 1% penicillin-streptomycin. Cells were incubated at 37 °C in a humidified atmosphere containing 5%  $\text{CO}_2$  and passaged every 3 days when monolayers at around 85% confluence were formed. Cell density was determined by counting the number of viable cells using trypan blue dye (Sigma-Aldrich) exclusion test. For passaging and plating, cells were detached using Tryple-Express (Invitrogen), stained using trypan blue, and loaded on the hemocytometer. All the experiments were done in triplicate.

**Studies of Cell Uptake.** CHO cells were seeded using supplemented DMEM (as described above) into 96-well plates and incubated for 24 h prior to the experiment. Nanoparticles were then added to the cells at different concentrations and the cells were incubated at 37 °C for 4 and 24 h. The experiment was terminated by washing the cell monolayer three times with (PBS) to eliminate excess particles not taken up by the cells. The cell membranes were permeabilized with 2% Triton X-100 to expose the internalized nanoparticles and allow quantitative measurement. Cell-associated nanoparticles were quantified by analyzing the cell lysate in an Infinite 200 PRO Microplate Reader (Tecan, Männedorf, Switzerland) and fluorescence was recorded at 673 nmEx/707 nmEm. Using fluorescence standard curves of polymeric nanoparticles, the recorded fluorescence data were then converted into amount of nanoparticles in terms of weight. Uptake was expressed as the amount of nanoparticles associated with the cells.

Nanoparticle uptake by the CHO cells was also investigated via confocal laser scanning microscopy. After incubation with nanoparticles for 24 h at a concentration of 1 mg/mL as described above, the cells were washed three times with PBS and fixed with 2% paraformaldehyde in PBS containing NucBlue fixed cell ready probe reagent (Thermo Fisher Scientific) for DAPI staining of cell nuclei. The cells were then imaged using a confocal laser scanning microscope (Zeiss LSM 710, Germany) equipped with an imaging software Zen 2011.

**Cytotoxicity Studies.** The cytotoxicity of polymeric nanoparticles was investigated *in vitro* using the calcein acetoxymethyl (AM) (Invitrogen) according to the manufacturer's instructions. The assay is based on the ability of living cells to convert nonfluorescent cell-permeant calcein AM to the intensely fluorescent calcein which can be read in a fluorescence spectrophotometer. The intensity of the fluorescence is proportional to the cell viability. Cells were seeded in a 96-well plate at  $1.5 \times 10^4$ /well and incubated for 24 h. The medium was then replaced with fresh medium containing polymeric nanoparticles at different concentrations and then the cells were incubated for 72 h. After the incubation period, the media containing nanoparticles was discarded, and the cells were washed three times with phosphate-buffered saline (PBS, pH 7.4). Calcein AM was then

added to the cells at 4  $\mu\text{M}$  and the cells were incubated for 60 min at 37 °C. The fluorescence was then recorded at 494 nmEx/517 nmEm. The cell viability was determined and expressed as a percentage of untreated control cells. Each sample was tested in triplicate.

**Characterization Techniques.**  $^1\text{H}$ -Nuclear Magnetic Resonance ( $^1\text{H}$  NMR),  $^1\text{H}$ - $^{13}\text{C}$  heteronuclear multiple-bond correlation ( $^1\text{H}$ - $^{13}\text{C}$  HMB), and  $^1\text{H}$ - $^{13}\text{C}$  heteronuclear single quantum coherence ( $^1\text{H}$ - $^{13}\text{C}$  HSQC) spectra were recorded using a Bruker Avance 400 MHz spectrometer at 25 °C. Deuterated dimethyl sulfoxide ( $\text{DMSO}-d_6$ ) and deuterated chloroform ( $\text{CDCl}_3$ ) were used as solvent for poly(OEGA-*co*-TFEA) and poly(OEGA-*co*-TFEA)-*b*-poly(St-*co*-VBA), respectively. All chemical shifts are reported in ppm ( $\delta$ ) relative to tetramethylsilane, referenced to the chemical shifts of residual solvent resonances.

$^{19}\text{F}$ -Nuclear Magnetic Resonance ( $^{19}\text{F}$  NMR).  $^{19}\text{F}$  NMR spectra were acquired using a Bruker Avance 400 MHz spectrometer with either  $\text{CDCl}_3$  or  $\text{H}_2\text{O}/\text{D}_2\text{O}$  (90/10, v/v) as solvent. Solution spectra were measured under the following measurements conditions: 90° pulse width 15  $\mu\text{s}$ , relaxation delay 1 s, acquisition time 0.73 and 128 scans.

$^{19}\text{F}$  spin–spin relaxation times ( $T_2$ ) were measured using the Carr–Purcell–Meiboom–Gill (CPMG) pulse sequence at 298 K. The samples were dissolved in  $\text{H}_2\text{O}/\text{D}_2\text{O}$  (90/10, v/v) at a concentration of 10 mg/mL. The 90° pulse was determined by dividing with a 360° pulse width, at which the NMR signal is zero. The relaxation delay was 1 s and the number of scans is 64. Only values for the major peaks are reported. For each measurement, the echo times were from 2 to 770 ms and 16 points were collected, which could be described by exponential functions for the calculation of  $T_2$ .

$^{19}\text{F}$  spin–lattice ( $T_1$ ) relaxation times were measured using the standard inversion–recovery pulse sequence. For each measurement, the relaxation delay was 2 s and the number of scans is 32. Only values for the major peaks are reported. For each measurement, the recovery times were from 2 ms to 3 s and 16 points were acquired. Values for the major peak at around  $-72.8$  ppm are reported.

$^1\text{H}$  and  $^{19}\text{F}$  MRI. Images of phantoms containing the polymer solutions were acquired on a Bruker BioSpec 94/30 USR 9.4 T small animal MRI scanner. Polymer solutions (10 mg/mL in  $\text{H}_2\text{O}$ ) were loaded in 5 mm NMR tubes, which were placed in a  $^1\text{H}/^{19}\text{F}$  dual resonator 40 mm volume coil.  $^1\text{H}$  were acquired for localization of the samples using a rapid acquisition with relaxation enhancement (RARE) sequence (rare factor = 16, TE = 88 ms, TR = 1500 ms, FOV = 40  $\times$  40 mm, matrix = 128  $\times$  128).  $^{19}\text{F}$  MRI images were acquired in the same stereotactic space as the  $^1\text{H}$  image using RARE sequence (rare factor = 32, TE = 11 ms, effective TE = 44 ms, TR = 1500 ms, number of averages = 128, FOV = 40  $\times$  40 mm, matrix = 64  $\times$  64, measurement time = 25 min 36 s). Only images for the major peaks were acquired.

**Size Exclusion Chromatography (SEC).** Number-average molecular weight ( $M_n$ , SEC) and dispersity ( $D = M_w/M_n$ ) of the synthesized polymers were measured using SEC performed on a Waters Alliance 2690 separations module equipped with a differential refractive index

(RI) detector. Analyte samples were dissolved in THF. Prior to injection, the samples were filtered through PTFE membranes (0.45  $\mu\text{m}$  pore size). THF was used as mobile phase at a flow rate of 1 mL  $\text{min}^{-1}$ . The molecular weights of the polymers were determined using Cirrus™ GPC software by a conventional calibration obtained from PS standards ranging from  $6.82 \times 10^2 \text{ g mol}^{-1}$  to  $1.67 \times 10^6 \text{ g mol}^{-1}$ .

**Dynamic Light Scattering (DLS).** DLS measurements were conducted using a Malvern Instrument Zetasizer nano series instrument equipped with a 4.0 mW He–Ne laser operating at 633 nm and a detection angle of  $173^\circ$ . The intensity weighted mean hydrodynamic diameter (Z-average) and the polydispersity factor were obtained from analysis of the autocorrelation functions using the method of cumulants. At least three measurements at  $25^\circ\text{C}$  were made for each sample with an equilibrium time of 2 min before starting measurement.

**Transmission Electron Microscopy (TEM).** TEM samples were prepared by depositing a drop of dilute sample (aggregate solutions were diluted with methanol at room temperature to generate 0.20% w/w dispersions) onto a carbon coated copper grid and dried at ambient temperature. TEM images were acquired using a JEOL 1010 electron microscope at an accelerating voltage of 100 kV.

## RESULTS AND DISCUSSION

The aim of this study is to develop a robust method for the preparation, in a one-pot reaction, of partly fluorinated polymeric nano-objects with a range of different morphologies. The secondary aim is to determine the effect of morphology on their uptake by cells, and to examine the potential of the nano-objects as  $^{19}\text{F}$  MRI contrast agents. The method of material preparation (see Scheme 1) relies on polymerization-induced self-assembly (PISA) occurring during the RAFT mediated dispersion polymerization. Statistical copolymers of OEGA and TFEA were prepared as macro RAFT agents, to provide a strong fluorine NMR/MRI signal and to control the chain extension with the second block in the heterogeneous PISA polymerization. The conditions required for the formation of nano-objects were investigated, and their behavior in *in vitro* cell culture was studied, with the objective to apply these polymers in  $^{19}\text{F}$  MRI.

**Design and Synthesis of OEGA and TFEA Copolymer as Macro RAFT Agent.**  $^{19}\text{F}$  MRI relies on the use of fluorinated contrast agents. An effective  $^{19}\text{F}$  MRI CA should fulfill several critical criteria, such as, (1) a single and narrow  $^{19}\text{F}$  resonance for maximum sensitivity and minimum imaging artifacts.<sup>8,24–26</sup> (2) high fluorine content for high sensitivity, (3) sufficiently long  $^{19}\text{F}$  spin–spin relaxation time ( $T_2$ ) to ensure the high signal-to-noise ratio (SNR) for optimal imaging,<sup>24,25</sup> and (4) the incorporation of multiple functionalities as a platform for the purpose of biological applications. In recent years, several groups of researchers have designed novel partly fluorinated polymers as  $^{19}\text{F}$  MRI CAs. These include linear polymers, star polymers, dendritic polymers, hyperbranched polymers, and meet the above-mentioned requirements by incorporating the fluorinated segments with other hydrophilic segments to maintain high mobility of the fluorine nuclei. A number of studies have been reported especially from our group. For instance, our fundamental studies of linear fluorinated copolymers of 2,2,2-trifluoroethyl acrylate (TFEA) and poly(ethylene glycol) methyl ether methacrylate (OEGMA) provide an important guidance for the design of  $^{19}\text{F}$  MRI CAs with complex architectures.<sup>27–29</sup> In addition, pH-responsive fluorinated star polymers based on the same monomers have been developed for tumor-selective imaging<sup>30,31</sup> and ion-responsive fluorinated contrast agents have been reported for the detection of cancer cells.<sup>32</sup> Thurecht et

al.<sup>33,34</sup> also reported the synthesis of PEG-based hyperbranched polymers (HBPs) using TFEA as the source of fluorine. These multifunctional polymers, combining one or more imaging multimodalities with a biocompatible, tunable and functional nanomaterial carrier, provide information on the tumor mass across various size scales *in vivo*, from millimeters down to tens of micrometres. Other groups, including Porsch et al.,<sup>35</sup> have reported the synthesis of dendritic doxorubicin (DOX) loaded core–shell nanoparticles using copolymers of OEGMA and 2,2,2-trifluoroethyl methacrylate (TFEMA) for MRI imaging and theranostic delivery to breast cancer cells.

Polymeric  $^{19}\text{F}$  imaging agents are desirable for preclinical and clinical studies because of the ability to incorporate a high fluorine content, their small size enabling for, e.g., tumor penetration, and the possibility of functionalization with additional imaging moieties or conjugated drugs. It is well-known that to achieve high MRI signal intensity, the fluorinated segments in the polymer structure should have a relatively long  $T_2$  and short  $T_1$ , as described by the following eq 3.<sup>36</sup>

$$I \approx N(F) \exp\left(\frac{-TE}{T_2}\right) \left[ 1 - 2 \exp\left(\frac{-(TR - \frac{TE}{2})}{T_1}\right) + \exp\left(\frac{-TE}{T_1}\right) \right] \quad (3)$$

where  $I$  is the imaging intensity,  $N(F)$  is the NMR detectable  $^{19}\text{F}$  nuclei density, and  $TR$ ,  $TE$  are the pulse sequence repetition time and echo delay times, respectively. The spin–spin relaxation time,  $T_2$ , is often the most crucial parameter and is determined by the strength of the dipolar coupling of the  $^{19}\text{F}$  nuclei with near neighbor fluorine and proton nuclei, and hence is sensitive to the spatial arrangement of the nuclear spins and their relative mobility. Therefore, care in the design of  $^{19}\text{F}$ -containing polymers is always necessary, because the fluorinated segments tend to aggregate in aqueous solution due to their hydrophobic nature, and this can significantly restrict local modes of motion leading to shortening of the  $T_2$  relaxation times,<sup>29,37</sup> which results in poor MRI signal-to-noise. Thus, to develop high performance imaging agents, the first and most important consideration is to prevent the association of the fluorinated segments.

The synthetic method adopted here, PISA in RAFT-mediated dispersion polymerization, is a powerful means to prepare core–shell structured particles with various morphologies including spheres, rods, worms, and vesicles. RAFT polymerization provides a method of synthesis of precisely defined polymers with diverse structure and a high level of functionality, even under heterogeneous polymerization conditions. The PISA process accordingly provides a robust synthetic route for the preparation of well-defined assemblies with controlled size and morphology at high concentrations without the need for further processing steps. Notable contributions to the field have been made by the research groups led by Armes,<sup>38–47</sup> Charleux,<sup>48,49</sup> and Pan et al.<sup>50–54</sup> For example, Armes has studied in detail the polymerization of 2-hydroxypropyl methacrylate (HPMA) in the presence of a dithiobenzoate-terminated PEG macro-RAFT agent. Spherical, worm-like and vesicle morphologies could be prepared through RAFT dispersion polymerization in water. Pan and his colleagues have mainly focused on nonaqueous dispersions

and published a series of articles describing the synthesis in an alcoholic medium of various morphologies with polystyrene as the core-forming block. On the other hand, Charleux has been concerned with RAFT emulsion polymerization, and has optimized various formulations in order to prepare nano-objects based on water-immiscible monomers such as styrene and *n*-butyl acrylate, with relatively high monomer conversions being achieved. Nano-objects such as nanospheres, nanofibers, and vesicles were obtained by varying the composition of the macro chain transfer agent, the pH and the salt concentration.<sup>55–58</sup>

In the course of the dispersion polymerization, particles nucleate when the solvophobic block reaches a critical block length. Subsequently, the core polymer extends and the initially formed spherical diblock copolymer particles may evolve toward other morphologies depending on not only molar mass, but also on particle stability, polymer segregation, and chain mobility. The structure of the macro-CTA is known to play an important role in control over the polymerization and achieving well-defined nanostructures.<sup>59</sup> Consequently, two issues need to be addressed. First, controlled/living behavior of the macro-CTA (i.e., no contamination with dead polymer chains) is critical not only for obtaining single particle morphology, but also for achieving successive morphology transitions during the polymerization. Second, when preparing particles from monomers having different reactivity, a high reinitiation efficiency from the macro-CTA is crucial to achieve good control over the polymerization during chain extension. In other words, the “more activated monomer” should be polymerized first such that the expelled radical is a similar or better homolytic leaving group with respect to the propagating radical of the second monomer (the “less activated monomer”).

In this work, our approach to limit aggregation of the fluorinated monomers is by statistical copolymerization of TFEA with OEGA using the RAFT technique (Scheme 1). The TFEA units within the particle shell provide the source of the <sup>19</sup>F NMR/MRI signal, while the OEGA units improve the water solubility, an approach commonly used in the preparation of biomaterials since PEG is hydrophilic, biocompatible, and approved by the United States Food and Drug Administration (FDA) for human use.<sup>60–62</sup> The structures of the poly(TFEA-*co*-OEGA) macro-CTAs were carefully characterized and discussed in terms of their livingness and reinitiation efficiency on the influence of morphology formation and transition. The core-shell structures were subsequently prepared by RAFT dispersion polymerization (PISA) St and VBA from the poly(TFEA-*co*-OEGA) macro-CTAs. St is commonly used in dispersion polymerization as a hydrophobic monomer in a block-selective solvent, and the gradual increase in the chain length of the insoluble block leads to the formation and transition of block copolymer assemblies. The VBA monomer incorporated into the polymer chain provides active groups, i.e., aldehyde, for further conjugation of the particles with functional dye molecules, to assist cell culture studies.

**Synthesis and Characterization of Poly(OEGA-*co*-TFEA) Macro-CTA.** Well-defined statistical copolymers of poly(OEGA-*co*-TFEA) macro-CTA were prepared by RAFT polymerization. As mentioned above, in order to achieve single morphology and successive morphology transitions in dispersion polymerization, our first target was to optimize the polymerization conditions for the production of well-defined poly(OEGA-*co*-TFEA) macro-CTA with high chain end fidelity. Previous studies from the Perrier group have shown

that high chain end functionality can be maintained despite reaching high monomer conversion, provided that reaction conditions are carefully chosen.<sup>63–65</sup> In a number of our previous studies, we performed the RAFT copolymerization of monomer OEG(M)A and TFEA in the presence of dithiobenzoate or trithiocarbonate RAFT agent with AIBN as initiator using the conventional RAFT recipe, [RAFT]: [AIBN] ratio of 5:1 in toluene at 65 °C for 24 h.<sup>27,28,31,66,67</sup> Monomer conversions of 50–80% could be attained after 8 h with relatively low molar mass dispersity of around 1.3. However, we also observed that the likelihood of side reactions increased with the long reaction times, resulting in the formation of dead chains with relatively broad molecular weight distributions especially for polymerizations involving OEGMA.<sup>22</sup> Furthermore, the large amount of initiator used can theoretically increase the fraction of dead chains, because the number of dead chains is only governed by the number of radicals generated throughout the polymerization in a degenerative transfer system such as RAFT.<sup>68</sup> Therefore, to limit the fraction of dead chains in this study, we conducted the RAFT polymerization at 60 °C in the presence of an extremely low concentration of initiator ([RAFT]:[Initiator] = 50:1) and replaced AIBN by VA-044 (half-life time of 10 h at 44 °C). At this temperature, VA-044 undergoes ~95% decomposition in 5 h compared to 85% for AIBN in 24 h. Using an initial monomer concentration ([OEGA]<sub>0</sub>) of 0.7 M (giving a workable solution viscosity) in a 20% dioxane aqueous solution (to facilitate solubilization of the CTA and TFEA monomer) and initiator concentration ([VA-044]<sub>0</sub>) of 7.0 × 10<sup>-4</sup> M we achieved >90% monomer conversion in 2 h. This low initiator concentration represents an initial ratio [CTA]<sub>0</sub>/[VA-044]<sub>0</sub> of 50, which theoretically leads to a very high fraction of living chains at the terminus of the macro-CTA (L ≈ 98.8%, calculated by eq 2). In addition, as shown in Figure 1, the values of *M*<sub>n,SEC</sub> and *D* (<1.2) as a function of conversion, and the observation of monomodal MWDs with a clear shift to higher molecular weights indicate that the polymerization is well controlled.

The second critical requirement of the macro-CTAs is a strong fluorine NMR signal and favorable relaxation properties. A series of poly(OEGA-*co*-TFEA) copolymers with different feed ratio of [OEGA]<sub>0</sub>:[TFEA]<sub>0</sub> were synthesized and characterized by <sup>19</sup>F NMR. As shown in Figure 2A, peaks at -74 to -75.2 ppm were observed in the <sup>19</sup>F NMR spectra of the copolymers and the chemical shift moved toward low ppm as the fluorine content increased. The shift to lower chemical shift is ascribed to sequence effects,<sup>28</sup> with longer runs of TFEA units present at higher fluorine contents. The spin-lattice relaxation (*T*<sub>1</sub>) and spin-spin relaxation (*T*<sub>2</sub>) times were determined by <sup>19</sup>F NMR. As displayed in Figure 2B and Table S1, when the fluorine content was increased from 2.2 to 13.9 wt %, *T*<sub>1</sub> decreased only slightly, while *T*<sub>2</sub> dropped significantly from 209 to 26 ms, which clearly indicates association of the fluorinated moieties in polymers with high fluorine content. The interplay between fluorine content and local dynamics, hence *T*<sub>2</sub> relaxation time, was discussed in detail in our previous studies.<sup>29,69</sup> In order to avoid the association of the fluorinated nano-objects for better <sup>19</sup>F MR imaging, in current study we prepared samples with a [OEGA]<sub>0</sub>:[TFEA]<sub>0</sub> feed ratio of 4:1 producing a macro-CTA with a fluorine content of 2.68 wt % and *T*<sub>2</sub> of 183 ms (Table S1).

The chemical structure of the poly(OEGA-*co*-TFEA) macro-CTA was also characterized by <sup>1</sup>H NMR spectroscopy. As

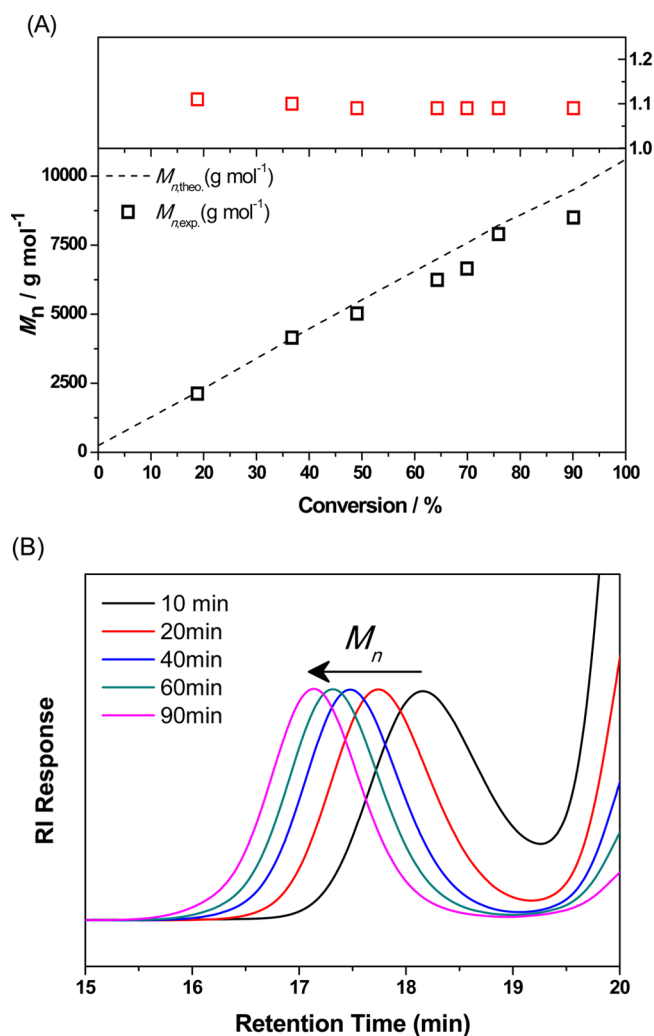


**Figure 1.** (A) Evolution of molecular weight and molar mass dispersity as a function of monomer conversion; (B) SEC chromatograms of poly(OEGA-co-TFEA) macro CTA obtained by RAFT polymerization at 60 °C in H<sub>2</sub>O:dioxane = 8:1. [OEGA]<sub>0</sub>: [TFEA]<sub>0</sub>: [CTBPA]<sub>0</sub>: [VA-044]<sub>0</sub> = 20:5:1:0.02. THF was used as the eluent.

shown in Figure 3A, all the characteristic peaks of TFEA, OEGA were identified and assigned. Specifically, the peaks at 4.5 and 4.2 ppm are from CH<sub>2</sub> adjacent to the ester bonds of TFEA and OEGA units, respectively. The dominant peak at ~3.6 ppm can be ascribed to the ethylene glycol (CH<sub>2</sub>CH<sub>2</sub>O) repeating units of OEGA side chains and the signals from the protons of the polymer backbone are located at 1.2–2.5 ppm. In addition, the peaks from the RAFT agent CTBPA were identified, confirming the retention of CTA functionality. <sup>13</sup>C NMR (Figure 3B) verified the chemical structure with all the relevant carbon peaks being observed. Notably, a small and broad resonance in the <sup>1</sup>H NMR spectrum centered at 4.8 ppm (inset in Figure 3A) was assigned to the methine protons from monomer units immediately adjacent to the trithiocarbonate group of the CTBPA RAFT agent.<sup>34</sup> <sup>1</sup>H–<sup>13</sup>C HSQC and <sup>1</sup>H–<sup>13</sup>C HMBP spectra were acquired to identify the carbons directly bonded to this proton at 4.8 ppm and the near neighbor atoms within a 4-bond distance. The HSQC spectrum in Figure S1A indicates that this peak has a one-bond heteronuclear correlation with a carbon peak at 50 ppm (indicated by the dotted line), which is attributed to a tertiary

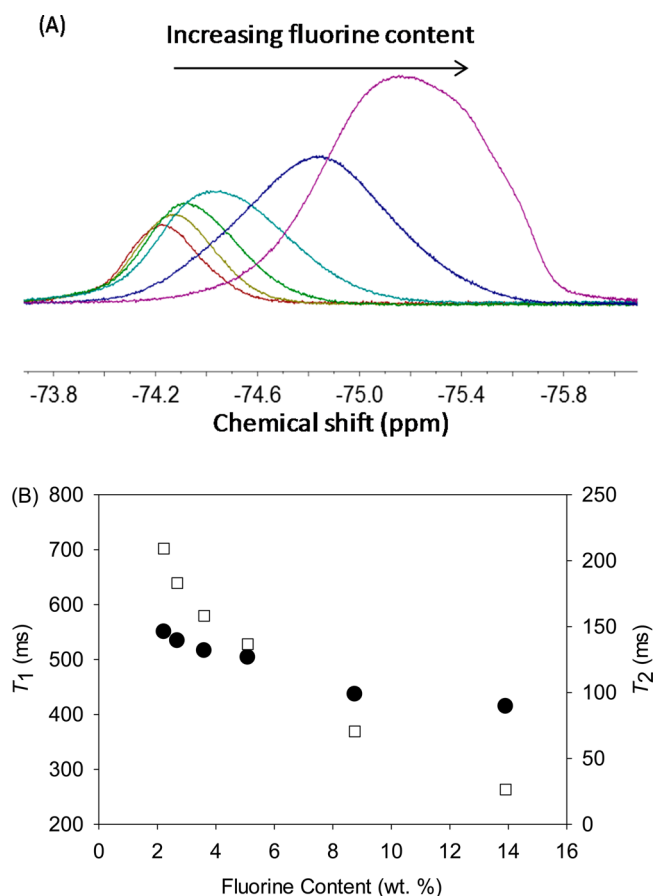


**Figure 2.** (A) Stacked <sup>19</sup>F NMR spectra in water of poly(OEGA-co-TFEA) with different fluorine contents (from left to right, 2.2, 2.7, 3.6, 5.1, 8.8, and 13.9 wt %). (B) T<sub>1</sub> (●) and T<sub>2</sub> (□) relaxation times of poly(OEGA-co-TFEA) with different fluorine contents. Samples were dissolved in H<sub>2</sub>O/D<sub>2</sub>O (90/10, v/v) at 20 mg mL<sup>-1</sup> at 25 °C.

carbon according to DEPT-135 <sup>13</sup>C NMR (SI, Figure S2). The HMBP spectrum (Figure S1B) also reveals that there is a four-bond heteronuclear correlation between the broad proton signal at 4.8 ppm and the carbons of the trithiocarbonate end group at 221.2 ppm (H1–C3), carbonyl groups at 170.4 ppm (H1–C2), methine (H1–C5) and methylene (H1–C4) from polymer backbone at 40.9 and 33.5 ppm. Furthermore, the <sup>13</sup>C nuclei from the carbonyl groups at 170.4 ppm are correlated with <sup>1</sup>H nuclei in CH<sub>2</sub> adjacent to the ester bonds of OEGA labeled as H6'–C2, indicating that the proton signal at 4.8 ppm should be assigned to the CH backbone of OEGA units immediately adjacent to the ω end-group of the polymer.

Quantification of the number of OEGA units adjacent to trithiocarbonate groups was achieved by <sup>1</sup>H and <sup>13</sup>C NMR analysis. The <sup>1</sup>H NMR spectrum suggests that 5 mol % of total OEGA (calculated from the integrals of 2e/(g+g')) units are located next to the ω end-group, while <sup>13</sup>C NMR analysis indicates a value of 6 mol % (calculated from the ratio of integrals of f/(g+g')) in the quantitative <sup>13</sup>C NMR). This result is in perfect accordance with the target ratio of [RAFT]: [OEGA], indicating that the terminal monomer group at the ω-end of the RAFT agent is exclusively OEGA and not TFEA.

**Synthesis of poly(OEGA-co-TFEA)-b-poly(St-co-VBA) Diblock Copolymer Nano-objects by RAFT Dispersion Polymerization.** The poly(OEGA-co-TFEA) macro-RAFT agents with low fractions of dead chains were subsequently

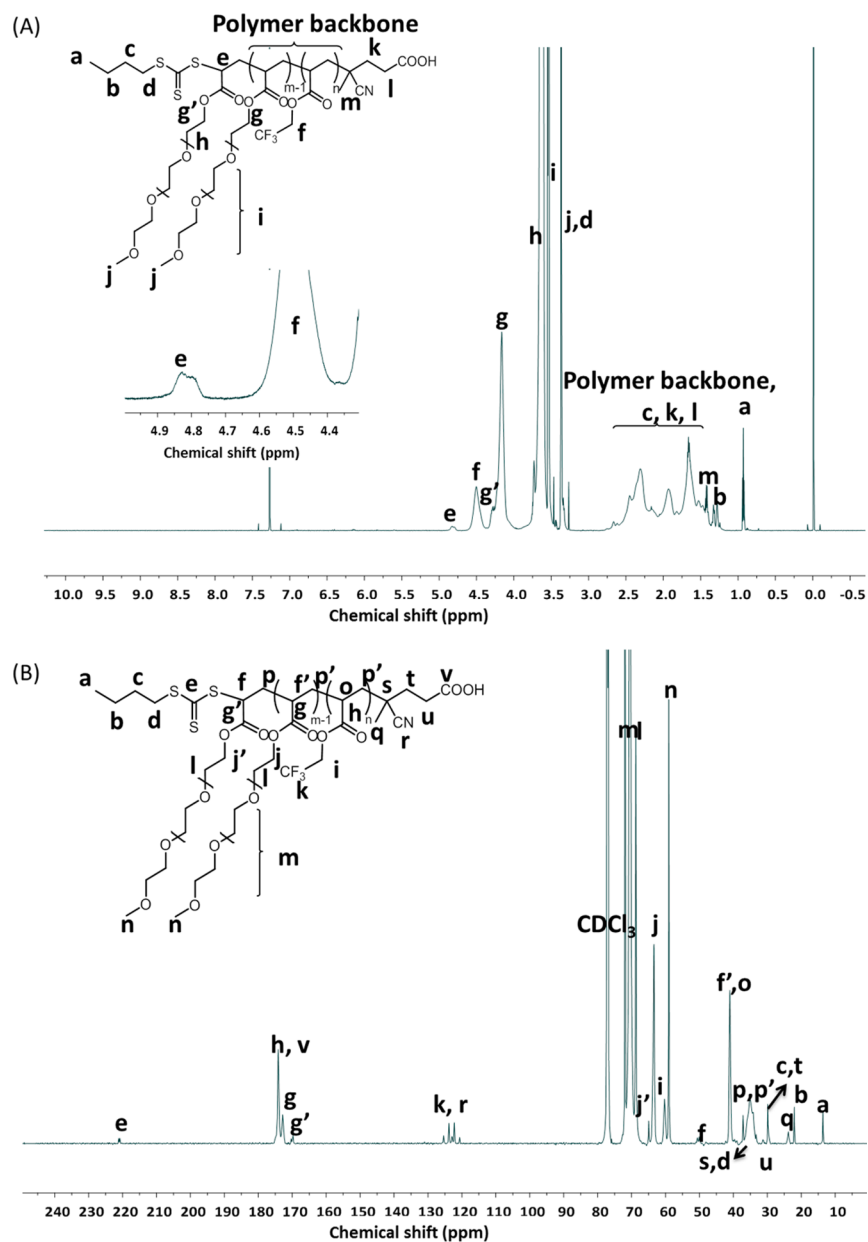


**Figure 3.** (A) <sup>1</sup>H NMR and (B) <sup>13</sup>C NMR spectra of poly(OEGA-co-TFEA) macro CTA in CDCl<sub>3</sub>. The inset in the proton spectrum shows an expansion of 4.3–5.0 ppm.

used in the RAFT dispersion copolymerization of styrene and 3-vinylbenzaldehyde using similar conditions as our previous study.<sup>22</sup> The polymerization were carried out at 90 °C with a molar ratio of [St]<sub>0</sub>: [VBA]<sub>0</sub>: [poly(OEGA-co-TFEA)]<sub>0</sub>: [VA-88]<sub>0</sub> = 4750:250:1:0.1 and styrene:isopropanol = 1:1 (wt:wt). The initial polymerization mixture was transparent since all ingredients are soluble in isopropanol. As the polymerization progressed, and when the length of the poly(St-co-VBA) block increased beyond a critical value, microphase separation occurred and the solution became turbid (Figure 4A). This occurred after 3 h reaction. As the polymerization proceeded further, the mixture turned opaque and finally white (Figure 4C–D), consistent with the formation of a dispersed phase comprising larger entities. The molecular weights increased with increasing conversion (Table 1), and the SEC chromatograms shown in Figure 5 moved toward high molecular weight with relatively narrow dispersity. The dispersity values

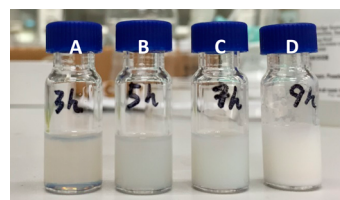


**Figure 4.** Digital photograph of RAFT dispersion polymerization mixtures with molar ratio of [St]<sub>0</sub>: [VBA]<sub>0</sub>: [poly(OEGA-co-TFEA)]<sub>0</sub>: [VA-88]<sub>0</sub> = 4750:250:1:0.1 and styrene:isopropanol = 1:1 (wt:wt) at different polymerization times: (A) 3 h, (B) 5 h, (C) 7 h, (D) 9 h.

increased at high conversions possibly due to termination and irreversible chain transfer reactions. The SEC traces in Figure 5 show that the macro-CTA was almost fully extended with the aromatic monomers, with only a small tail present at low molecular weights. This observation indicates a relatively high

**Table 1. Summary of the RAFT Dispersion Block Copolymerization of Styrene and Vinyl Benzaldehyde in the Presence of Poly(OEGA-co-TFEA) as a Macro-CTA**

time (h)	VBA conv. (%)	St conv. (%)	$M_n$ (NMR) $\text{g mol}^{-1}$	$M_n$ (SEC) $\text{g mol}^{-1}$	$D$
3 h	5.7	4.4	37 200	27 910	1.49
5 h	9.1	11.3	72 300	46 100	1.43
7 h	16.2	17.2	103 600	76 700	1.42
9 h	28.8	22.5	133 700	115 200	1.61

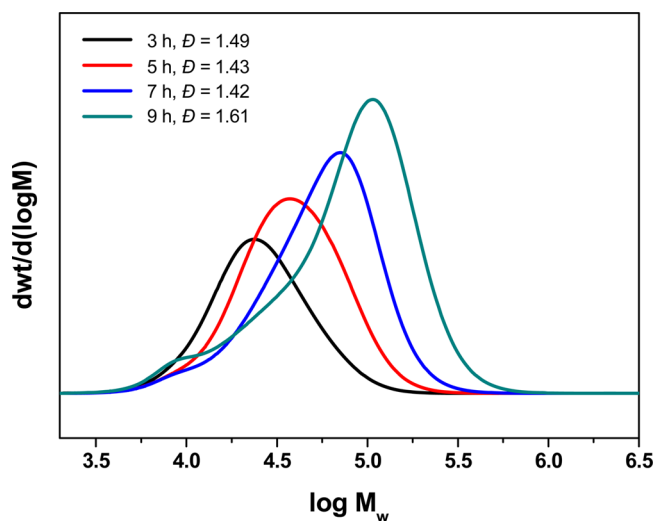


**Figure 5.** Evolution of SEC traces ( $w(\log M)$  vs  $\log M$ ) with conversion in dispersion polymerization of styrene in isopropanol at 90 °C with poly(OEGA-co-TFEA) as macro CTA.

reinitiation efficiency of the poly(OEGA-co-TFEA) macro CTA and confirms the high chain end fidelity of the first block.

**Characterization of the in Situ Formed Poly[(OEGA-co-TFEA)]-*b*-poly(St-co-VBA) Nano-objects.** The morphology of the poly[(OEGA-co-TFEA)]-*b*-poly(St-co-VBA) nano-objects was investigated using transmission electron microscopy. Samples were prepared following the procedure described in the literature.<sup>70,71</sup> The nano-objects were first dispersed in methanol at 0.1 wt % and dried on a carbon-coated copper grid under air. The TEM images (Figure 6) showed that core functional asymmetric block copolymer aggregates first formed spherical micelles after 3 h, and subsequently, worm-like vesicles and then spherical vesicles at increasing polymerization times. The changes in morphology are governed by the length of the poly(St-co-VBA) chains. Spherical particles of diameter ~60 nm were formed when the number-average degree of polymerization ( $DP_n$ ) of the poly(St-co-VBA) block reached approximately 220 units. A transition in morphology from micelles to worm-like structures was observed for poly(St-co-VBA) blocks greater than 560 repeating units, while vesicles with diameter 150–500 nm were formed when  $DP_n$  of the second block reached over 800. Finally, a longer poly(St-co-VBA) block ( $DP = 1140$ ) caused the vesicles to aggregate and form large compound vesicles with an average diameter of 1–2  $\mu\text{m}$ . The evolution in morphology was also followed by DLS. Figure 8 shows the size distributions based on intensity of the copolymer assemblies A–D, which is in accordance with the TEM observations. Notably, in this work, pure morphologies were obtained at each point during the polymerization, which implies high structural homogeneity of the diblock copolymers

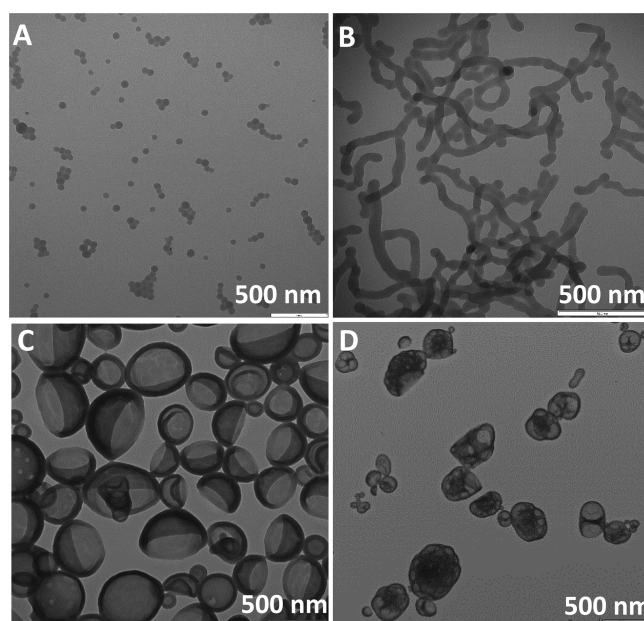


**Figure 6.** TEM images of nano-objects from RAFT dispersion polymerization with molar ratio  $[\text{St}]_0:[\text{VBA}]_0:[\text{poly}(\text{OEGA-co-TFEA})]_0:[\text{VA-88}]_0 = 4750:250:1:0.1$  and styrene:isopropanol = 1:1 (wt:wt) for different polymerization times: (A) 3 h (St conv. 4.4%), (B) 5 h (11%), (C) 7 h (17%), (D) 9 h (22%). Samples were prepared by dilution with methanol to generate 0.2% w/w dispersions.

with good control over the polymerization. We also note that the final morphology, determined by the phase separation during polymerization, does not appear to be significantly affected by the solvents used in subsequent steps (precipitation and conjugation). Finally, the presence of aldehyde groups in the core of the nano-objects was exploited to conjugate dye molecules for the purpose of the biological studies. The morphologies after dye conjugation were also characterized by TEM, and the results showed no obvious changes in the nanoparticle size and shape after the coupling reaction with the dye (Figure S3). The DMSO used in the conjugation reaction presumably swelled the core to some extent, allowing the dye molecule access to the aldehyde groups. This process apparently did not disrupt the nanoparticle morphology.

**$^{19}\text{F}$  NMR and MRI of the Fluorinated Nano-objects.** In order to evaluate their potential as  $^{19}\text{F}$  MRI contrast agents, the partly fluorinated nano-objects with morphologies of spheres, worm-like particles, and vesicles were examined by  $^{19}\text{F}$  NMR. Samples were dispersed in  $\text{D}_2\text{O}$  at a concentration of 10  $\text{mg mL}^{-1}$  with TFA as an internal  $^{19}\text{F}$  reference. As can be seen in Figure 7, all the  $^{19}\text{F}$  NMR spectra exhibited a single peak at  $-73.2$  ppm. The intensity of the peak was seen to decrease as the fluorine content decreased in order of spherical particles, worm-like particles, and vesicles. Furthermore, the  $^{19}\text{F}$  NMR relaxation times  $T_1$  and  $T_2$  of the nano-objects were measured and listed in Table 2.  $T_1$  and  $T_2$  relaxation times remained constant for all nano-objects, showing no dependence on morphology. This result indicates that the structure and dynamics of the hydrophilic shell of nano-objects are not affected significantly by changes in the overall morphology of the nanoparticles.

The final aim of this work is to examine the potential of the nano-objects as  $^{19}\text{F}$  MRI agents.  $^{19}\text{F}$  MRI of the fluorinated nano-objects was conducted in  $\text{H}_2\text{O}$  at 10  $\text{mg/mL}$  using a

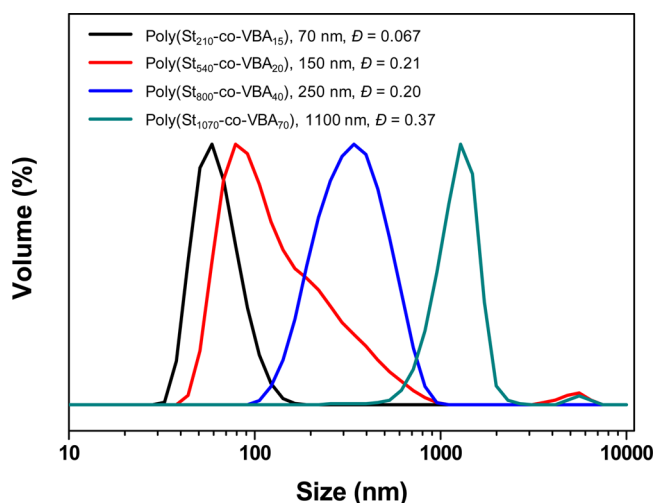


**Figure 7.** DLS results of the poly[(OEGA-co-TFEA)]-*b*-poly(St-co-VBA) block copolymer aggregates obtained from RAFT dispersion polymerization with molar ratio  $[St]_0:[VBA]_0:[poly(OEGA-co-TFEA)]_0:[VA-88]_0 = 4750:250:1:0.1$  and styrene:isopropanol = 1:1 (wt:wt) for different polymerization times (black: 3 h, red: 5 h, blue: 7 h, and green: 9 h).

**Table 2.** NMR Properties of the Fluorinated Polymeric Nano-objects in D<sub>2</sub>O

sample morphology	fluorine content (wt %)	$[^{19}F]$ (mM)	$^{19}F$ NMR $T_1/T_2$	$^{19}F$ MRI intensity ( $\times 10^6$ ) (ms)
spherical particles	0.26	1.4	538/176	8.09
worm-like particles	0.13	0.68	537/176	7.41
vesicles	0.09	0.47	536/179	5.39

spin-echo pulse sequence. The acquisition parameters were kept constant, and the signal-to-noise ratio (SNR) of the MR images was measured under identical conditions.  $^1H$  RARE images displayed on the left were used to locate the NMR tubes within the resonator. All of the samples could be detected successfully through  $^{19}F$  MRI and the images are shown in Figure 8B. As shown above (Table 2) the  $T_1$  and  $T_2$  relaxation times do not appear to be sensitive to the morphology, therefore, the  $^{19}F$  MRI intensity should be proportional to the detectable fluorine content. The  $^{19}F$  MRI intensities (expressed as a signal-to-noise ratio, SNR) calculated from the  $^{19}F$  MRI images are listed in Table 2. The spherical particles with the highest fluorine content (0.26 wt %) and smallest particle size in H<sub>2</sub>O solution gave the highest  $^{19}F$  MRI SNR. The signal-to-

noise ratio was not, however, strictly proportional to the fluorine content of the solutions, with the intensity of the spherical particles being lower than expected. This indicates that segmental motion of a proportion of the fluorinate segments in the coronas of these particles is restricted to some extent. However, the relaxation time measurements and the MRI intensities further show that the dynamics of the observed signals for the partly fluorinated poly[(OEGA-co-TFEA)] chains in the particle coronas experience the same dynamics irrespective of the shape of the core of the particles.

**Uptake of the Nano-objects by Cells.** Morphologies other than spherical have recently attracted attention for biological applications. For example, long and flexible worm-like particles were found to have significantly longer blood circulation times *in vivo* compared to their spherical analogues.<sup>72</sup> On the other hand, short rods have potential for application in a range of areas, as a consequence of their unusual rheological<sup>73–75</sup> and gelation properties.<sup>76–78</sup> The other class of structures, the vesicles, are promising for drug delivery since drugs can be loaded and protected inside the cargo and released in response to an applied or endogenous trigger.<sup>79</sup> Of more relevance to this study, the shape of nanosized particles has long been known to affect the rate and extent of uptake by cells.<sup>14–18</sup> In those reviews it is reported that for particles with identical surface chemistry, rod-shaped particles were taken up by cells more rapidly than particles of other geometry, although conflicting results have been reported, since factors such as aspect ratio and mean dimensions must be taken into account.

In our study, the effect of particle morphology on particle uptake into CHO cells was examined by incubation of solutions of the three different polymeric nanoparticles with the cells for 4 and 24 h. The influence of concentration of particles in solution was also examined. At different time points the cells were analyzed by fluorescence spectroscopy to assess the extent of uptake of the nanoparticles (Figure 9). This figure clearly shows that at all time points the worm-like nanoparticles showed the highest uptake, and vesicle nanoparticles were less likely to be taken up by the cells. Previous studies of cell uptake of both hard-core nanoparticles and soft nanoparticles are consistent with our findings.<sup>80–84</sup> For example, Tang et al. found that silica nanoparticles with worm and rod-like shapes showed greater adhesion of nanoparticles to the cell membrane due to their higher surface area of contact, an important parameter for high cell uptake.<sup>82</sup> Others have reported that rod-like polymeric particles were taken up to a higher extent than their spherical counter parts.<sup>80,84</sup> Very recently Hinde and colleagues<sup>85</sup> used Pair correlation microscopy of similar

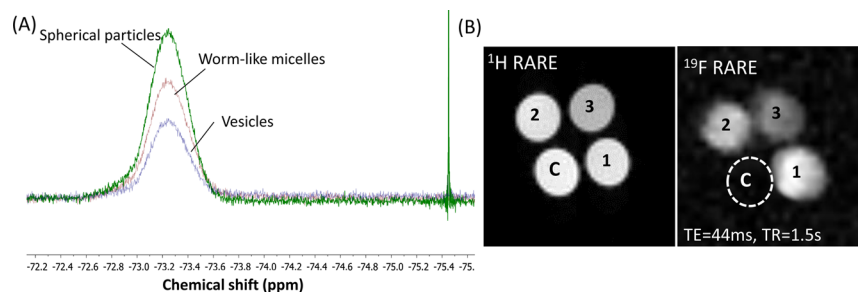


**Figure 8.**  $^{19}F$  NMR and  $^{19}F$  MRI of nano-objects with different morphologies. (A)  $^{19}F$  NMR of samples at concentration of 10 mg/mL. (B) phantom images of the samples using 9.4 T  $^{19}F$  MRI (1: spherical particles, 2: worm-like particles, 3: vesicles and c: control). Note that  $^1H$  RARE imaging was performed to localize the sample vials.

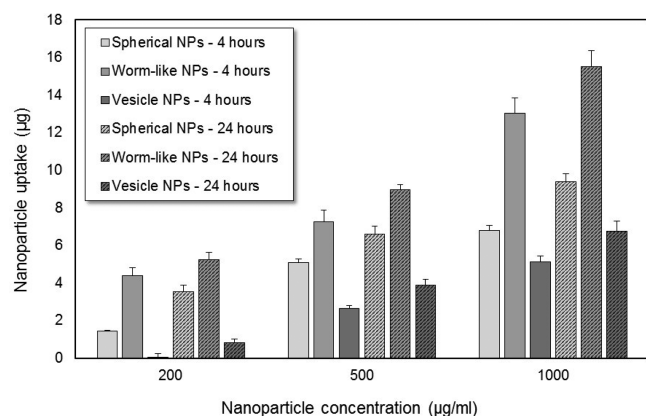


**Figure 9.** Extent of uptake by CHO cells of particles having different morphology measured using fluorescence spectroscopy at different time points (4 and 24 h).

nanoparticles to those examined here and also found that particles of larger aspect ratio, i.e., rods and worms entered MCF7 cells more readily than spherical particles. This collective data, and the results of the current study, suggest that the higher aspect ratio of worm or rod-like nanoparticles compared to spherical nanoparticles results in a larger contact surface with the cell membranes, which then promotes cell uptake. Note that confocal microscopy confirmed the accumulation of the nanoparticles in the cytoplasm for all the different morphological nanoparticles (Figure 10).

**Cytotoxicity Studies.** The cytotoxicity of the polymeric nanoparticles with different morphologies was tested on a CHO cell line. The cells were incubated with the polymers for 72 h and the cell viability was assessed using the calcein AM assay. Live cells are distinguished by the presence of intracellular esterase activity, determined by the enzymatic conversion of the virtually nonfluorescent cell-permeant calcein AM to the intensely fluorescent calcein. Nonviable cells rapidly lose metabolic capacity and thus do not generate a fluorescence signal. As seen in Figure 11, the viability of CHO cells was not affected by the spherical nanoparticles at any tested concentrations. The cells appeared to be slightly sensitive to vesicle nanoparticles at high concentration (1 mg/mL) (cell viability  $\sim 96 \pm 1\%$ ). Slightly higher toxicity of worm-like nanoparticles on CHO cells was observed compared to nanoparticles of other morphology, especially at higher concentrations. An increase in uptake of these nanoparticles may have a more profound effect on the cells. Nevertheless, the viability of the cells after incubation with worm-like nano-

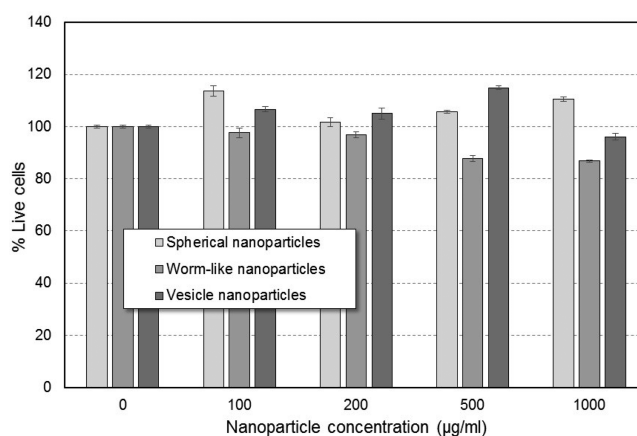


**Figure 11.** Viability of CHO cells after incubation with different polymeric nanoparticles at different concentrations for 24 h. The results are the average of three replicates  $\pm$  standard deviation.

particles for 72 h was above 80%. Therefore, these three nanoparticles of different morphology are regarded as nontoxic under the conditions tested. In summary, the low levels of cytotoxicity of the nanoparticles tested on CHO cell line can be ranked as follows: spherical nanoparticles > vesicle nanoparticles > worm-like nanoparticles.

## CONCLUSIONS

In summary, we have synthesized a range of novel fluorinated diblock copolymer of poly(OEGA-*co*-TFEA)-*b*-poly(St-*co*-VBA) nano-objects (spheres, worm-like particles and vesicles) directly through a one-pot RAFT dispersion polymerization. As expected, these nano-objects show detectable  $^{19}\text{F}$  MRI signal with sensitivity increasing as fluorine content increases in order of spheres > worm-like particles > vesicles. The  $^{19}\text{F}$  NMR relaxation time  $T_1$  and  $T_2$  values were independent of the morphology of the nano-objects, indicating that the dynamics of the corona of the particles was the same for the different morphologies. Using CHO cells, we demonstrated a significant effect of morphology on cell uptake with the highest uptake observed for worm-like structures. All nanoparticles displayed little or no cytotoxicity. The results demonstrate that nano-objects with specific morphology, and decorated with partly fluorinated hydrophilic coronas have great potential for loading and imaging of cells and potentially for *in vivo* cell tracking. Further experiments in this direction are being conducted, and will be reported subsequently

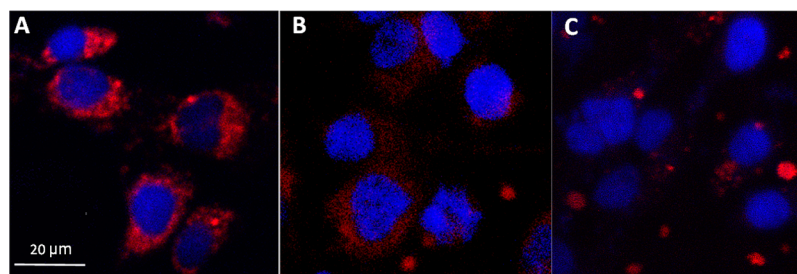


**Figure 10.** Confocal laser scanning microscopy showing uptake by CHO cells of different shaped nano-objects, (A) micelles, (B) worm-like particles, and (C) vesicles after 24 h of incubation. (Note that the extent of conjugation of the spherical nanoparticles with fluorophores was greater than for the worm-like particles, and thus a stronger fluorescence signal was observed for these particles. The reason for this is not known; however, the calculation of the extent of uptake took into account the different level of dye loading.)

## ■ ASSOCIATED CONTENT

### Supporting Information

The Supporting Information is available free of charge on the ACS Publications website at DOI: 10.1021/acs.biomac.6b01788.

<sup>1</sup>H–<sup>13</sup>C HSQC and HMBC spectrum of poly((OEGA-co-TFEA) macro CTA in CDCl<sub>3</sub>, DEPT-135 C NMR spectrum of poly(PEGA-co-TFEA) macro CTA in CDCl<sub>3</sub>, and TEM images of nano-objects after conjugation with Cy5.5 dye (PDF)

## ■ AUTHOR INFORMATION

### Corresponding Author

\*E-mail: a.whittaker@uq.edu.au.

### ORCID

Hang T. Ta: 0000-0003-1188-0472

Andrew K. Whittaker: 0000-0002-1948-8355

### Present Address

Australian Institute for Bioengineering and Nanotechnology, University of Queensland, Brisbane City, QLD 4072, Australia

### Notes

The authors declare no competing financial interest.

## ■ ACKNOWLEDGMENTS

W.Z. and C.Z. were supported by the Australian Research Council (CE140100036) and National Health and Medical Research Council (AP1037310). The authors would also like to acknowledge the Australian National Fabrication Facility (Queensland Node); National Imaging Facility, Centre for Advanced Imaging for access to key items of equipment.

## ■ REFERENCES

- (1) Lauterbur, P. C. *Nature* **1973**, *242* (5394), 190–191.
- (2) Bottrill, M.; Kwok, L.; Long, N. J. *Chem. Soc. Rev.* **2006**, *35* (6), 557–571.
- (3) Bellin, M. F. *Eur. J. Radiol.* **2006**, *60* (3), 314–323.
- (4) Lauterbur, P. C. *Angew. Chem., Int. Ed.* **2005**, *44* (7), 1004–1011.
- (5) Pan, D.; Lanza, G. M.; Wickline, S. A.; Caruthers, S. D. *Eur. J. Radiol.* **2009**, *70* (2), 274–285.
- (6) Verdijk, P.; Scheenen, T. W. J.; Lesterhuis, W. J.; Gambarota, G.; Veltien, A. A.; Walczak, P.; Scharenborg, N. M.; Bulte, J. W. M.; Punt, C. J. A.; Heerschap, A.; Figdor, C. G.; de Vries, I. J. M. *Int. J. Cancer* **2007**, *120* (5), 978–984.
- (7) Ruiz-Cabello, J.; Barnett, B. P.; Bottomley, P. A.; Bulte, J. W. M. *NMR Biomed.* **2011**, *24* (2), 114–129.
- (8) Knight, J. C.; Edwards, P. G.; Paisey, S. J. *RSC Adv.* **2011**, *1* (8), 1415–1425.
- (9) Chen, J.; Lanza, G. M.; Wickline, S. A. *Wiley Interdisciplinary Reviews: Nanomedicine and Nanobiotechnology* **2010**, *2* (4), 431–440.
- (10) Holland, G.; Bottomley, P.; Hinshaw, W. J. *Magn. Reson.* **1977**, *28* (1), 133–136.
- (11) O'Reilly, R. K.; Hawker, C. J.; Wooley, K. L. *Chem. Soc. Rev.* **2006**, *35* (11), 1068–1083.
- (12) Hawker, C. J.; Wooley, K. L. *Science* **2005**, *309* (5738), 1200–1205.
- (13) Hubbell, J. A.; Chilkoti, A. *Science* **2012**, *337* (6092), 303–305.
- (14) Kamaly, N.; Xiao, Z.; Valencia, P. M.; Radovic-Moreno, A. F.; Farokhzad, O. C. *Chem. Soc. Rev.* **2012**, *41* (7), 2971–3010.
- (15) Mao, Z.; Zhou, X.; Gao, C. *Biomater. Sci.* **2013**, *1* (9), 896–911.
- (16) Daum, N.; Tscheka, C.; Neumeyer, A.; Schneider, M. *Wiley Interdiscip. Rev. Nanomed. Nanobiotechnol.* **2012**, *4* (1), 52–65.
- (17) Duan, X.; Li, Y. *Small* **2013**, *9* (9–10), 1521–1532.
- (18) Arnida; Janát-Amsbury, M. M.; Ray, A.; Peterson, C. M.; Ghandehari, H. *Eur. J. Pharm. Biopharm.* **2011**, *77* (3), 417–423.
- (19) Mai, Y.; Eisenberg, A. *Chem. Soc. Rev.* **2012**, *41* (18), 5969–5985.
- (20) Chiefari, J.; Chong, Y. K.; Ercole, F.; Krstina, J.; Jeffery, J.; Le, T. P. T.; Mayadunne, R. T. A.; Meijs, G. F.; Moad, C. L.; Moad, G.; Rizzardo, E.; Thang, S. H. *Macromolecules* **1998**, *31* (16), 5559–5562.
- (21) Moad, G.; Rizzardo, E.; Thang, S. H. *Acc. Chem. Res.* **2008**, *41* (9), 1133–1142.
- (22) Zhao, W.; Gody, G.; Dong, S. M.; Zetterlund, P. B.; Perrier, S. *Polym. Chem.* **2014**, *5* (24), 6990–7003.
- (23) Gody, G.; Maschmeyer, T.; Zetterlund, P. B.; Perrier, S. *Nat. Commun.* **2013**, *4*, 2505.
- (24) Janjic, J. M.; Ahrens, E. T. *Wiley Interdiscip. Rev. Nanomed. Nanobiotechnol.* **2009**, *1* (5), 492–501.
- (25) Yu, Y. B. *Wiley Interdiscip. Rev. Nanomed. Nanobiotechnol.* **2013**, *5* (6), 646–661.
- (26) Srinivas, M.; Heerschap, A.; Ahrens, E. T.; Figdor, C. G.; de Vries, I. J. M. *Trends Biotechnol.* **2010**, *28* (7), 363–370.
- (27) Zhang, C.; Peng, H.; Whittaker, A. K. *J. Polym. Sci., Part A: Polym. Chem.* **2014**, *52* (16), 2375–2385.
- (28) Zhang, C.; Peng, H.; Puttick, S.; Reid, J.; Bernardi, S.; Searles, D. J.; Whittaker, A. K. *Macromolecules* **2015**, *48* (10), 3310–3317.
- (29) Peng, H.; Blakey, I.; Dargaville, B.; Rasoul, F.; Rose, S.; Whittaker, A. K. *Biomacromolecules* **2009**, *10* (2), 374–381.
- (30) Wang, K.; Peng, H.; Thurecht, K. J.; Puttick, S.; Whittaker, A. K. *Polym. Chem.* **2014**, *5* (5), 1760–1771.
- (31) Wang, K. W.; Peng, H.; Thurecht, K. J.; Puttick, S.; Whittaker, A. K. *Polym. Chem.* **2013**, *4* (16), 4480–4489.
- (32) Zhang, C.; Moonshi, S. S.; Peng, H.; Puttick, S.; Reid, J.; Bernardi, S.; Searles, D. J.; Whittaker, A. K. *ACS Sensors* **2016**, *1* (6), 757–765.
- (33) Rolfe, B. E.; Blakey, I.; Squires, O.; Peng, H.; Boase, N. R. B.; Alexander, C.; Parsons, P. G.; Boyle, G. M.; Whittaker, A. K.; Thurecht, K. J. *J. Am. Chem. Soc.* **2014**, *136* (6), 2413–2419.
- (34) Ardana, A.; Whittaker, A. K.; Thurecht, K. J. *Macromolecules* **2014**, *47* (15), 5211–5219.
- (35) Porsch, C.; Zhang, Y.; Östlund, Å.; Damberg, P.; Ducani, C.; Malmström, E.; Nyström, A. M. *Part. Part. Syst. Char.* **2013**, *30* (4), 381–390.
- (36) Hendrick, R. E.; Kneeland, J. B.; Stark, D. D. *Magn. Reson. Imaging* **1987**, *5*, 117–127.
- (37) Janjic, J. M.; Srinivas, M.; Kadayakkara, D. K. K.; Ahrens, E. T. *J. Am. Chem. Soc.* **2008**, *130* (9), 2832–2841.
- (38) Lovett, J. R.; Ratcliffe, L. P. D.; Warren, N. J.; Armes, S. P. *Macromolecules* **2016**, *49* (8), 2928–2941.
- (39) Canning, S. L.; Smith, G. N.; Armes, S. P. *Macromolecules* **2016**, *49* (6), 1985–2001.
- (40) Hanisch, A.; Yang, P. C.; Kulak, A. N.; Fielding, L. A.; Meldrum, F. C.; Armes, S. P. *Macromolecules* **2016**, *49* (1), 192–204.
- (41) Derry, M. J.; Fielding, L. A.; Armes, S. P. *Prog. Polym. Sci.* **2016**, *52*, 1–18.
- (42) Ratcliffe, L. P. D.; McKenzie, B. E.; Le Bouedec, G. M. D.; Williams, C. N.; Brown, S. L.; Armes, S. P. *Macromolecules* **2015**, *48* (23), 8594–8607.
- (43) Lopez-Oliva, A. P.; Warren, N. J.; Rajkumar, A.; Mykhaylyk, O. O.; Derry, M. J.; Doncom, K. E. B.; Rymaruk, M. J.; Armes, S. P. *Macromolecules* **2015**, *48* (11), 3547–3555.
- (44) Warren, N. J.; Mykhaylyk, O. O.; Ryan, A. J.; Williams, M.; Doussineau, T.; Dugourd, P.; Antoine, R.; Portale, G.; Armes, S. P. *J. Am. Chem. Soc.* **2015**, *137* (5), 1929–1937.
- (45) Gonzato, C.; Semsarilar, M.; Jones, E. R.; Li, F.; Krooshof, G. J. P.; Wyman, P.; Mykhaylyk, O. O.; Tuinier, R.; Armes, S. P. *J. Am. Chem. Soc.* **2014**, *136* (31), 11100–11106.
- (46) Warren, N. J.; Armes, S. P. *J. Am. Chem. Soc.* **2014**, *136* (29), 10174–10185.
- (47) Ladmiral, V.; Semsarilar, M.; Canton, I.; Armes, S. P. *J. Am. Chem. Soc.* **2013**, *135* (36), 13574–13581.
- (48) Qiao, X. G.; Lansalot, M.; Bourgeat-Lami, E.; Charleux, B. *Macromolecules* **2013**, *46* (11), 4285–4295.

- (49) Charleux, B.; Delaittre, G.; Rieger, J.; D'Agosto, F. *Macromolecules* **2012**, *45* (17), 6753–6765.
- (50) Wan, W. M.; Pan, C. Y. *Macromolecules* **2010**, *43* (6), 2672–2675.
- (51) Sun, J. T.; Hong, C. Y.; Pan, C. Y. *Soft Matter* **2012**, *8* (30), 7753–7767.
- (52) Wan, W. M.; Sun, X. L.; Pan, C. Y. *Macromol. Rapid Commun.* **2010**, *31* (4), 399–404.
- (53) Wan, W. M.; Hong, C. Y.; Pan, C. Y. *Chem. Commun.* **2009**, 39, 5883–5885.
- (54) Wan, W. M.; Pan, C. Y. *Polym. Chem.* **2010**, *1* (9), 1475–1484.
- (55) Chaduc, I.; Crepet, A.; Boyron, O.; Charleux, B.; D'Agosto, F.; Lansalot, M. *Macromolecules* **2013**, *46* (15), 6013–6023.
- (56) Zhang, W. J.; D'Agosto, F.; Dugas, P. Y.; Rieger, J.; Charleux, B. *Polymer* **2013**, *54* (8), 2011–2019.
- (57) Boisse, S.; Rieger, J.; Pembouong, G.; Beaunier, P.; Charleux, B. *J. Polym. Sci., Part A: Polym. Chem.* **2011**, *49* (15), 3346–3354.
- (58) Zhang, X. W.; Boisse, S.; Zhang, W. J.; Beaunier, P.; D'Agosto, F.; Rieger, J.; Charleux, B. *Macromolecules* **2011**, *44* (11), 4149–4158.
- (59) Rieger, J. *Macromol. Rapid Commun.* **2015**, *36* (16), 1458–1471.
- (60) Huynh, V. T.; de Souza, P.; Stenzel, M. H. *Macromolecules* **2011**, *44* (20), 7888–7900.
- (61) Cho, H. Y.; Srinivasan, A.; Hong, J.; Hsu, E.; Liu, S.; Shrivats, A.; Kwak, D.; Bohaty, A. K.; Paik, H.-j.; Hollinger, J. O.; Matyjaszewski, K. *Biomacromolecules* **2011**, *12* (10), 3478–3486.
- (62) Soeriyadi, A. H.; Li, G.-Z.; Slavin, S.; Jones, M. W.; Amos, C. M.; Becer, C. R.; Whittaker, M. R.; Haddleton, D. M.; Boyer, C.; Davis, T. P. *Polym. Chem.* **2011**, *2* (4), 815–822.
- (63) Zetterlund, P. B.; Gody, G.; Perrier, S. *Macromol. Theory Simul.* **2014**, *23* (5), 331–339.
- (64) Gody, G.; Maschmeyer, T.; Zetterlund, P. B.; Perrier, S. *Macromolecules* **2014**, *47* (10), 3451–3460.
- (65) Gody, G.; Maschmeyer, T.; Zetterlund, P. B.; Perrier, S. *Nat. Commun.* **2013**, *4*, 4.
- (66) Wang, K. W.; Peng, H.; Thurecht, K. J.; Puttick, S.; Whittaker, A. K. *Polym. Chem.* **2016**, *7* (5), 1059–1069.
- (67) Wang, K. W.; Peng, H.; Thurecht, K. J.; Puttick, S.; Whittaker, A. K. *Biomacromolecules* **2015**, *16* (9), 2827–2839.
- (68) Zhong, M.; Matyjaszewski, K. *Macromolecules* **2011**, *44* (8), 2668–2677.
- (69) Peng, H.; Thurecht, K. J.; Blakey, I.; Taran, E.; Whittaker, A. K. *Macromolecules* **2012**, *45* (21), 8681–8690.
- (70) He, W.-D.; Sun, X.-L.; Wan, W.-M.; Pan, C.-Y. *Macromolecules* **2011**, *44* (9), 3358–3365.
- (71) Zhang, X.; Rieger, J.; Charleux, B. *Polym. Chem.* **2012**, *3* (6), 1502–1509.
- (72) Geng, Y.; Dalhaimer, P.; Cai, S. S.; Tsai, R.; Tewari, M.; Minko, T.; Discher, D. E. *Nat. Nanotechnol.* **2007**, *2* (4), 249–255.
- (73) Dreiss, C. A. *Soft Matter* **2007**, *3* (8), 956–970.
- (74) Oelschlaeger, C.; Waton, G.; Buhler, E.; Candau, S. J.; Cates, M. E. *Langmuir* **2002**, *18* (8), 3076–3085.
- (75) Zhang, W. J.; Charleux, B.; Cassagnau, P. *Macromolecules* **2012**, *45* (12), 5273–5280.
- (76) Huang, Z.; Lee, H.; Kang, S. K.; Nam, J. M.; Lee, M. *Nat. Commun.* **2011**, *2*, 459.
- (77) Blanz, A.; Verber, R.; Mykhaylyk, O. O.; Ryan, A. J.; Heath, J. Z.; Douglas, C. W. I.; Armes, S. P. *J. Am. Chem. Soc.* **2012**, *134* (23), 9741–9748.
- (78) Groison, E.; Brusseau, S.; D'Agosto, F.; Magnet, S.; Inoubli, R.; Couvreur, L.; Charleux, B. *ACS Macro Lett.* **2012**, *1* (1), 47–51.
- (79) Karagoz, B.; Esser, L.; Duong, H. T.; Basuki, J. S.; Boyer, C.; Davis, T. P. *Polym. Chem.* **2014**, *5* (2), 350–355.
- (80) Alemdaroglu, F. E.; Alemdaroglu, N. C.; Langguth, P.; Herrmann, A. *Macromol. Rapid Commun.* **2008**, *29*, 326–329.
- (81) Arnida, A.; Malugin, A.; Ghandehari, H. *J. Appl. Toxicol.* **2010**, *30*, 212–217.
- (82) Huang, X.; Teng, X.; Chen, D.; Tang, F.; He, J. *Biomaterials* **2010**, *31*, 438–448.
- (83) Lesniak, A.; Salvati, A.; Santos-Martinez, M. J.; Radomski, M. W.; Dawson, K. A.; Åberg, C. *J. Am. Chem. Soc.* **2013**, *135*, 1438–1444.
- (84) Karagoz, B.; Esser, L.; Duong, H. T.; Basuki, J. S.; Boyer, C.; Davis, T. P. *Polym. Chem.* **2014**, *5* (2), 350–355.
- (85) Hinde, E.; Thammasiraphop, K.; Duong, H. T. T.; Yeow, J.; Karagoz, B.; Boyer, C.; Gooding, J. J.; Gaus, K. *Nat. Nanotechnol.* **2017**, *12* (1), 81–89.

**Supporting Information to**

**Polymerization-Induced Self-Assembly (PISA) -Control over the**

**Morphology of <sup>19</sup>F-containing Polymeric Nano-objects for Cell**

**Uptake and Tracking**

Wei Zhao<sup>1,2</sup>, Hang T. Ta<sup>1,2</sup>, Cheng Zhang,<sup>1,2</sup> Andrew K. Whittaker<sup>1,2,\*</sup>

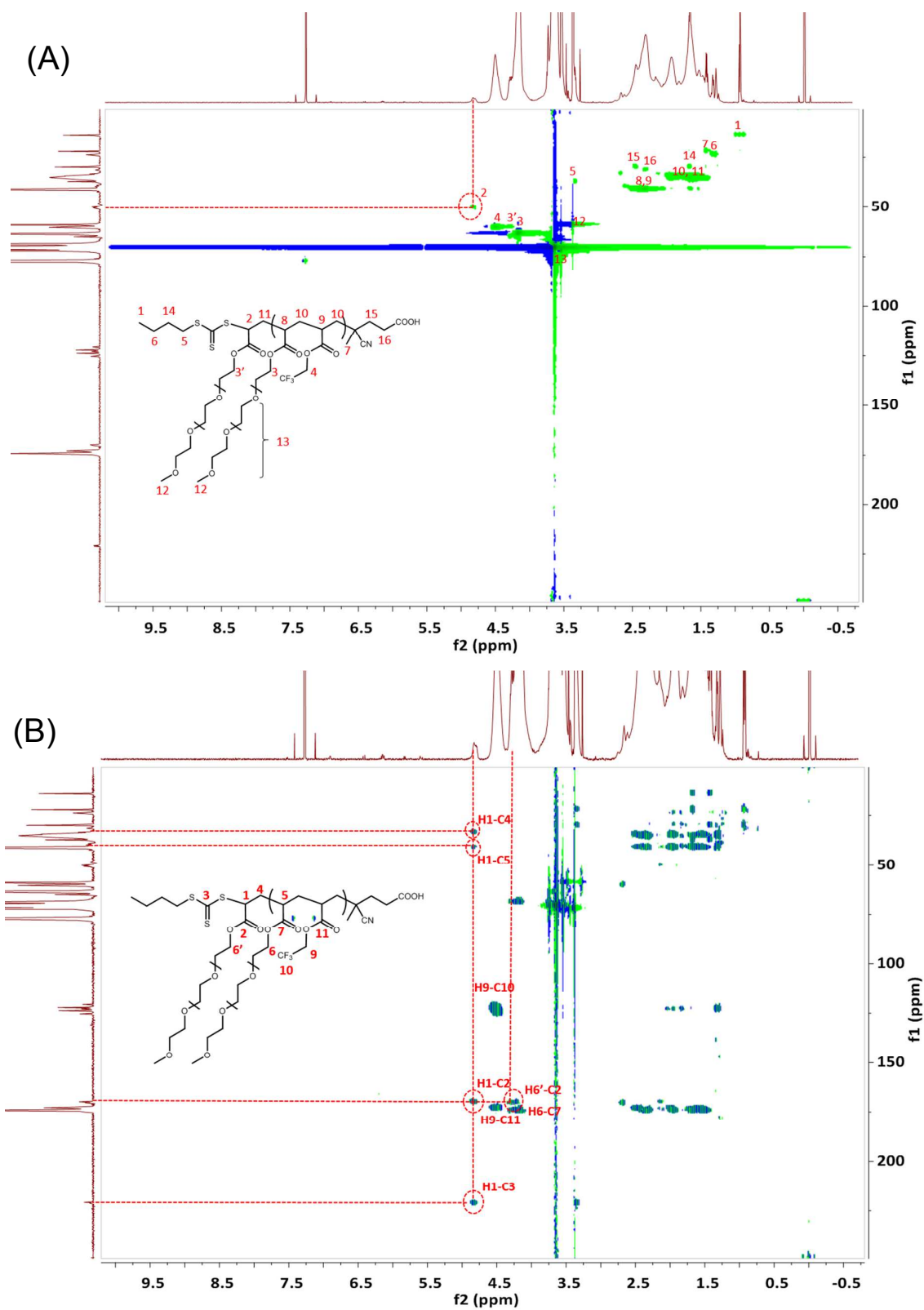
<sup>1</sup>Australian Institute for Bioengineering and Nanotechnology, The University of Queensland, Brisbane, St Lucia QLD 4072, Australia

<sup>2</sup>ARC Centre of Excellence in Convergent Bio-Nano Science and Technology

\*Correspondence to: A. Whittaker (E-mail: [a.whittaker@uq.edu.au](mailto:a.whittaker@uq.edu.au))

**Table S1.**  $T_1$  and  $T_2$  relaxation times in water of poly(OEGA-*co*-TFEA) with different fluorine contents at a polymer concentration of 20 mg mL<sup>-1</sup> at 25 °C.

Entry	[OEGA] <sub>0</sub> : [TFEA] <sub>0</sub> feed ratio	<sup>19</sup> F content (wt.%)	$T_1$ (ms)	$T_2$ (ms)
1	5:1	2.22	550.6	209.2
2	4:1	2.68	534.6	183.0
3	3:1	3.6	516.3	158.2
4	2:1	5.09	504.2	136.7
5	1:1	8.75	436.8	70.5
6	1:2	13.91	414.7	26.4



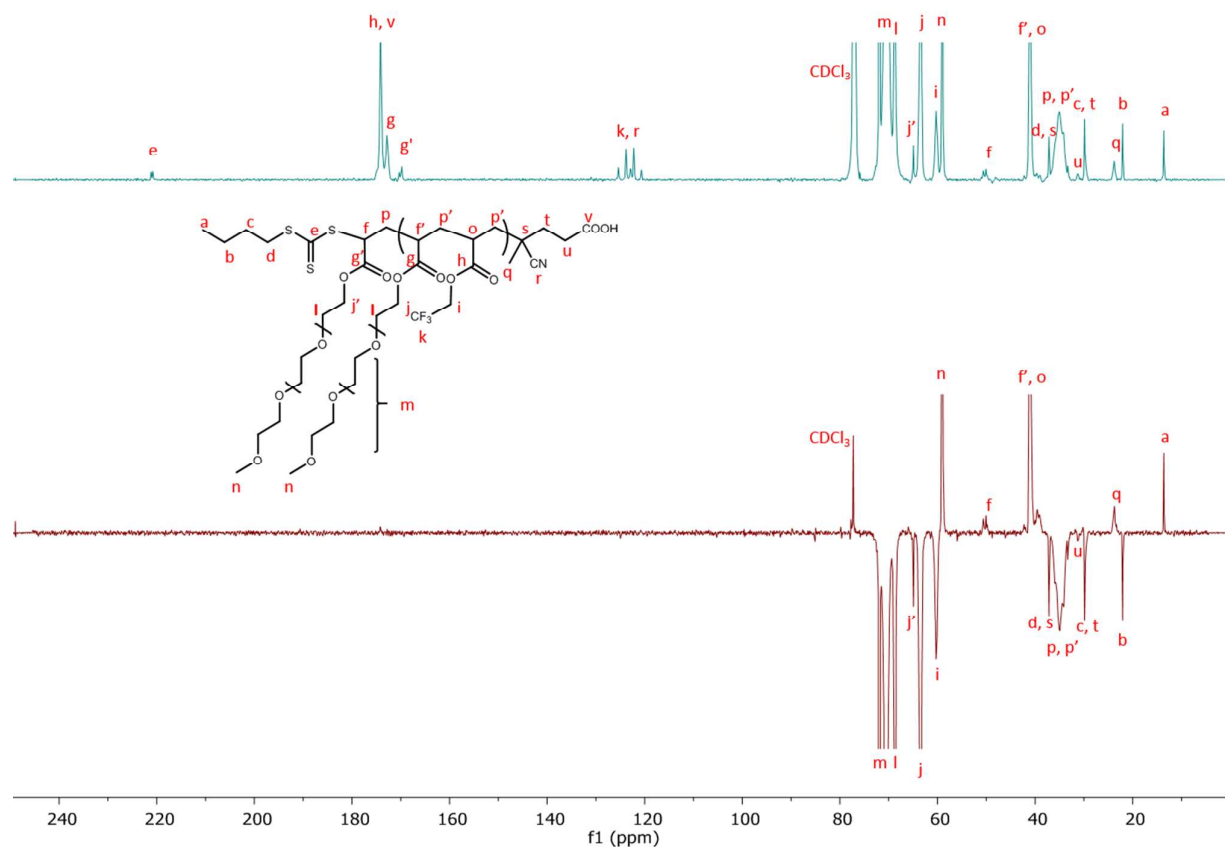


**Figure S2.** DEPT-135 C NMR spectrum of poly(PEGA-*co*-TFEA) macro CTA in CDCl<sub>3</sub>.

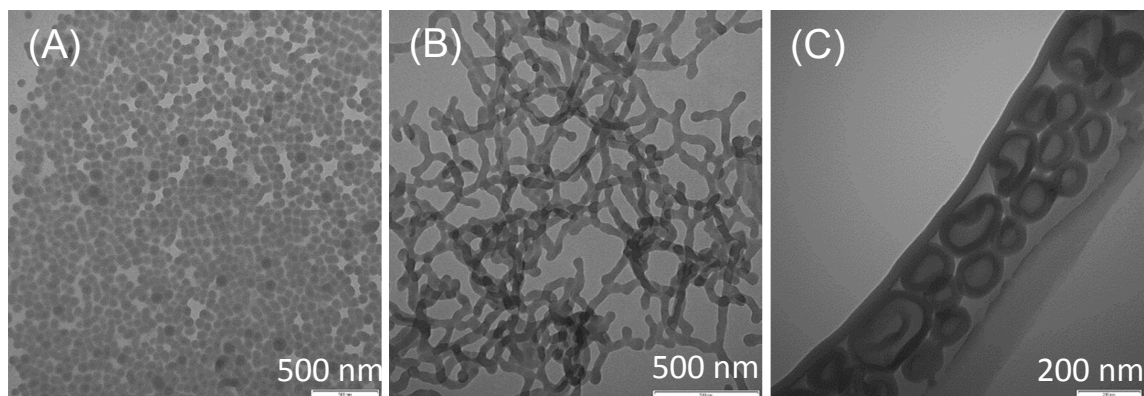


**Figure S3.** TEM images of nano-objects prepared with different polymerization times after conjugation with Cy5.5 dye: (A) 3h, (B) 5h and (C) 7h.